FOCUS ISSUE

MULTIFUNCTIONAL HALIDE PEROVSKITES

Single- or double A-site cations in $A_3Bi_2I_9$ bismuth perovskites: What is the suitable choice?

Feray Ünlü[1], Ashish Kulkarni[2], Khan Lê[1], Christoph Bohr[1], Andrea Bliesener[3], Seren Dilara Öz[1], Ajay Kumar Jena[4], Yoichi Ando[3], Tsutomu Miyasaka[4], Thomas Kirchartz[2,5], Sanjay Mathur[1,a)]

[1] Department for Chemistry, Institute of Inorganic Chemistry, University of Cologne, Greinstr. 6, 50939 Cologne, Germany
[2] IEK5-Photovoltaics, Forschungszentrum Jülich, 52425 Jülich, Germany
[3] Physics Institute II, University of Cologne, Zülpicher Str. 77, 50937 Cologne, Germany
[4] Graduate School of Engineering, Toin University of Yokohama, Aoba, Yokohama 225-8503, Japan
[5] Faculty of Engineering and CENIDE, University of Duisburg-Essen, Carl-Benz-Str. 199, 47057 Duisburg, Germany
a) Address all correspondence to this author. e-mail: sanjay.mathur@uni-koeln.de

Investigations on the effect of single or double A-site cation engineering on the photovoltaic performance of bismuth perovskite-inspired materials ($A_3Bi_2I_9$) are rare. Herein, we report novel single- and double-cation based bismuth perovskite-inspired materials developed by (1) completely replacing $CH_3NH_3^+$ (methylammonium, MA^+) in $MA_3Bi_2I_9$ with various organic cations such as $CH(NH_2)_2^+$ (formamidinium, FA^+), $(CH_3)_2NH_2^+$ (dimethylammonium, DMA^+), $C(NH_2)_3^+$ (guanidinium, GA^+) and inorganic cations such as cesium (Cs^+), rubidium (Rb^+), potassium (K^+), sodium (Na^+) and lithium (Li^+) and (2) partially replacing MA^+ with Cs^+ in different stoichiometric ratios. Compared to single-cation based bismuth perovskite devices, the double-cation bismuth perovskite device showed an increment in the device power conversion efficiency (PCE) up to 1.5% crediting to the reduction in the bandgap. This is the first study demonstrating double-cation based bismuth perovskite showing bandgap reduction and increment in device efficiency and opens up the possibilities towards compositional engineering for improved device performance.

Introduction

Organic–inorganic hybrid perovskite solar cells have gained significant attention due to a rapid rise in power conversion efficiency (PCE) from 3.8% to beyond 25% in less than one decade [1, 2]. In addition to this, exciting optoelectronic properties such as suitable and tuneable bandgap [3], long charge-carrier lifetimes [4, 5], relatively low recombination activity at interfaces [6, 7], sufficiently high mobilities of both charge carriers, and high defect-tolerance [8], have enabled the application of perovskite materials in various optoelectronic devices. Nevertheless, such high-performing perovskite devices are not always compatible with sufficient durability of the device, which is mainly affected by external factors like moisture, light, heat, and intrinsic factors such as ion migration, defects, and hydrophilic organic cations [9]. This leads to the degradation of the photoactive perovskite material to non-photoactive lead iodide which is inherently

toxic [10]. Efforts have been made to improve the stability via interface engineering, compositional engineering, development of multi-dimensional (2D + 3D) perovskites, etc. [9, 11–13]. Among all these approaches, compositional engineering has been at the forefront of research efforts as it not only helps to develop a robust perovskite composition but also helps in tuning its optoelectronic properties [9, 14, 15]. For instance, the replacement of the methylammonium (MA^+) cation in $MAPbI_3$ with formamidinium ($CH(NH_2)_2^+$, FA^+) to form $FAPbI_3$ simultaneously increases thermal stability up to 150 °C and reduces the bandgap (E_g) from 1.55 to 1.47 eV enabling a wider absorption of the solar spectrum [16, 17]. In addition to this, the development of inorganic perovskites (e.g.: $CsPb(I_xBr_{1-x})_3$) has garnered significant attention because of their inorganic nature, high thermal stability up to 350 °C, and wide E_g which is useful for tandem devices [18, 19]. To date, most of the top-performing

cells showing efficiency beyond 20% are employing perovskite absorber layers with multi A-site cations. These absorber layers combine rather large organic cations such as FA^+, MA^+ with slightly smaller inorganic cations such as Cs^+, K^+ and thereby achieve improved stability and optoelectronic performance. Although their certified efficiency is still improving, the toxicity of lead (Pb) and the possible bioaccumulation in the ecosystem has increased concerns and may not be suitable for commercialization [20]. Therefore, developing eco-friendly perovskite-inspired materials that conserve all properties of lead-based perovskites but without lead (Pb) is critical. In this regard, tin (Sn) based perovskite materials have been developed showing the efficiency of up to 10% for $CsFASnI_3$ composition [21]. However, Sn-perovskites suffer from rapid oxidation of Sn^{2+} to Sn^{4+}, which hampers the device efficiency and long-term stability of the cell [22].

Since lead (Pb^{2+}) and bismuth (Bi^{3+}) cations share an isoelectronic $6s^2$ state, bismuth is considered as a non-toxic alternative to lead. Bismuth-based perovskite-inspired materials with an $A_3B_2X_9$ (A = MA^+, Cs^+, B = Bi^{3+}, X = I^-, Br^-) structure show exceptional stability against moisture and heat compared to lead-based perovskites. In addition to this, bismuth perovskite-inspired materials show promising semiconducting, electronic, optical, and ferroelectric properties [23]. In 2015, Park et al. reported $Cs_3Bi_2I_9$ and $MA_3Bi_2I_9$ based mesoscopic heterojunction solar cells yielding power conversion efficiency (PCE) of 1.09% for the former and 0.2% for the latter [24]. Subsequently, efforts have been made to further improve the efficiency by employing suitable electron transport layers [25], vapour deposition [26], solvent engineering [27]; however, the efficiency has been limited. Nevertheless, various solution-based and vapor-assisted methods were reported with different solvents [27, 28] and fabrication processes leading to PCEs between 0.01% [29] and 1.64% [30]. Efforts have also been made to develop bismuth perovskite with alternative A-site cations. For instance, replacing Cs^+ with Rb^+ or K^+ as A-site cations were reported to influence the crystal structure and bandgap character, however, the device showed PCE of less than 1% [31].

$Cs_3Bi_2I_9$ and $MA_3Bi_2I_9$ crystallize in the hexagonal $P6_3/mmc$ space group with face-sharing binuclear $(Bi_2I_9)^{3-}$ octahedra isolated and surrounded by the Cs^+ or MA^+ cations and are described as zero-dimensional (0D) structures [32]. They possess a wide indirect bandgap (> 2.0 eV) [33] and high exciton binding energy (70–270 meV) [24], thus limiting the transport of photogenerated charge carriers. However, replacing Cs^+ with Rb^+ or K^+ ($Rb_3Bi_2I_9$ and $K_3Bi_2I_9$) leads to two-dimensional (2D) structures with direct band gaps and improved charge transport properties [31]. Replacement of MA^+ with pyridinium cations, as demonstrated by Li et al., resulted in a pseudo-3D structure with $(BiI_4)^-$ chains, lowering of the bandgap (1.78 eV) and improvement in PCE up to 0.9% [34]. Although compositional

engineering manifested to help in tuning the dimensional structure, optoelectronic properties, and thereby device efficiency of Pb-based perovskites, most of the reports on Bi-based materials have employed either $Cs_3Bi_2I_9$ or $MA_3Bi_2I_9$ absorber in the solar cells. Less attention has been devoted towards the development of various single- or double- A-site cation based bismuth perovskite inspired materials.

Herein, we report A-site cation engineering in bismuth perovskites by replacing MA^+ with various organic cations such as $CH(NH_2)_2^+$ (formamidinium, FA^+), $(CH_3)_2NH_2^+$ (dimethylammonium, DMA^+), $C(NH_2)_3^+$ (guanidinium, GA^+) and inorganic alkali metal cations such as lithium (Li^+), potassium (K^+), rubidium(Rb^+), cesium (Cs^+) and perform a comparative investigation on the structural, morphological, optical and photovoltaic device properties of the resultant bismuth iodide compounds. Further, for the first time, we fabricated double-cation Cs^+/MA^+ based bismuth iodide thin films and investigated the structural, morphological, optical, and photovoltaic device properties. Among the various perovskite-inspired materials explored, it was interesting to observe that the single-cation based bismuth perovskite demonstrated PCEs up to 0.24% while the double A-site cation based bismuth perovskite showed enhancement in the device efficiency up to 1.5%. This is attributed to the flat morphology on the mesoporous TiO_2 layer and bandgap narrowing. This study opens up the door to compositionally designed bismuth perovskite-inspired materials based on double A-site cation rendering for improved device performance.

Results and discussion

Single-cation based bismuth perovskites

Figure 1 shows various organic and inorganic A-site cations employed to fabricate bismuth perovskite thin films and a schematic illustration of either the zero-dimensional (0D) or two dimensional (2D) layered crystal structure and device architecture. All perovskite solutions were prepared by stirring BiI_3 and the desired organic or inorganic cation (as shown in Fig. 1) in a ratio of 2:3 in dimethylformamide (DMF) at room temperature for 30 min. The stoichiometry for the solid composition is derived from the solution composition. The solutions were spin-coated on mesoporous TiO_2 coated fluorine-doped tin oxide (FTO) substrates followed by annealing at 100 °C to obtain orange-red colored thin films (photographs of the thin films are presented in Figure S1 in the supplementary information). In addition to this, toluene was used as an anti-solvent during spin-coating to enhance the crystallinity. The thin-film and device fabrication steps are detailed in the section materials and methods. The crystal structures of bismuth perovskite materials obtained with various organic and inorganic cations were analyzed by X-ray diffraction (XRD) and the results are

shown in Fig. 2. The pattern of $MA_3Bi_2I_9$ matches the hexagonal $P6_3/mmc$ space group [35] with preferred orientation along the (011) ($2\theta = 12.6°$) plane on mesoporous TiO_2 coated on FTO substrate (Fig. 2a black trace and Figure S2). In comparison to $MA_3Bi_2I_9$, $FA_3Bi_2I_9$ shows a similar XRD pattern to $MA_3Bi_2I_9$ with a preferential orientation along the (011) plane (Fig. 2a, blue trace) and is in line with the previous report by Lan et al. [29] For the $DMA_3Bi_2I_9$ case, there is a slight shift of all peaks towards smaller 2θ angles, which is most probably due to the larger ionic radius of the DMA^+ compared to MA^+ cation ($r_{DMA+} = 272$ pm vs. $r_{MA+} = 217$ pm) (Fig. 2a, cyan trace). Additionally, it shows a preferred orientation along (010) ($2\theta = 11.8°$) and new doublets at $2\theta \sim16°$, 18°, and 20°, which could belong to an unknown phase. In the case of the larger guanidinium cation ($r_{GA+} = 278$ pm), the pattern fits the orthorhombic Cmcm space group [36] with face-shared and isolated bioctahedrons (Fig. 2a, magenta trace and Figure S3).

$Cs_3Bi_2I_9$ crystallizes in the hexagonal $P6_3/mmc$ group (Fig. 2b, black trace and Figure S4) which is consistent with $MA_3Bi_2I_9$ having a zero-dimensional structure with isolated bioctahedrons [24]. Employing rubidium as cation resulted in the monoclinic space group $P2_1/n$ and a 2D layered vacancy-ordered structure. The thin film pattern, as shown in Fig. 2b with blue trace and Figure S5, is in agreement with the crystal structure reported by Lehner et al. [31] The highest intensity peak can be seen at $2\theta = 25.5°$ revealing a preferred orientation of the polycrystalline thin film along the (00-6) direction. In case of $K_3Bi_2I_9$ perovskite thin film, it shows similarity to the pattern of $Rb_3Bi_2I_9$ (Fig. 2b, cyan trace) with most intense peaks at $2\theta = 8.4°$ and 18.1° which can be assigned to the (00-2) and the (004) plane, respectively. Additionally, these peaks are shifted to higher angles compared to $Rb_3Bi_2I_9$ due to the smaller ionic radius of K^+ ($r_{Rb+} = 149$ pm vs. $r_{K+} = 138$ pm). In the pattern of $Na_3Bi_2I_9$, additionally to the (00-2) and (00-4) planes, we observed a third peak equidistant to the former which may originate from the (006) plane. Due to the similarity to the previous patterns (Fig. 2b, magenta trace), we assume that $K_3Bi_2I_9$

and $Na_3Bi_2I_9$ form a 2D layered structure. In the case of $Li_3Bi_2I_9$, which formed a yellow thin film (Figure S1), we suspect that the structure might have collapsed most probably due to a much smaller ionic radius ($r_{Li+} = 76$ pm) compared to the other alkali metals, showing a different pattern with peaks at $2\theta = \sim 8°$, 16°, 24°, 32° and 40°.

The optical properties were investigated by UV–vis absorption spectroscopy which is displayed in Fig. 3. All obtained thin films exhibit a strong absorption peak at 500 nm which is ascribed to an intrinsic exciton absorption caused by the transition from the $^1S_0$ to $^3P_1$ state in the Bi^{3+} cation [32, 37]. In the case of $K_3Bi_2I_9$ there is an additional peak at 550 nm, which might result from additional gap states within the bandgap. The extracted direct and indirect band gaps were derived from Tauc Plots (Figures S6 and S7). Here, the excitonic band edge was also considered, which we named as excitonic bandgap. Our calculated direct optical band gap of 2.9 eV for $MA_3Bi_2I_9$ (Table S1) is in line with density functional theory calculations ($E_g = 2.94$ eV), which were reported earlier by our group [32]. All extrapolated optical band gaps are listed in Table S1 and Table S2, showing that generally, the direct band gaps are higher than 2.0 eV, whereas $MA_3Bi_2I_9$ has the widest and $K_3Bi_2I_9$ and $Cs_3Bi_2I_9$ the lowest (2.3 eV). This indicates that the A-site cation has an impact on the bandgap of the perovskite-inspired bismuth halide materials. Such bandgap tuning is also observed in lead halide perovskites because of the structural fluctuations in the lead halide framework caused by A-site cation engineering [9]. Lower dimensional materials usually have wide band gaps and strong confinement effects, which can hinder electronic charge transport [38]. The obtained perovskites exhibit 0D (perovskite-inspired) or 2D (vacancy-ordered perovskite) crystal structures with wide band gaps (the crystal structure of the perovskite materials is shown in ESI along with the XRD pattern). Despite this, the application in solar cell devices is still interesting as they could be employed as lead-free alternatives in perovskite-perovskite tandem solar cells.
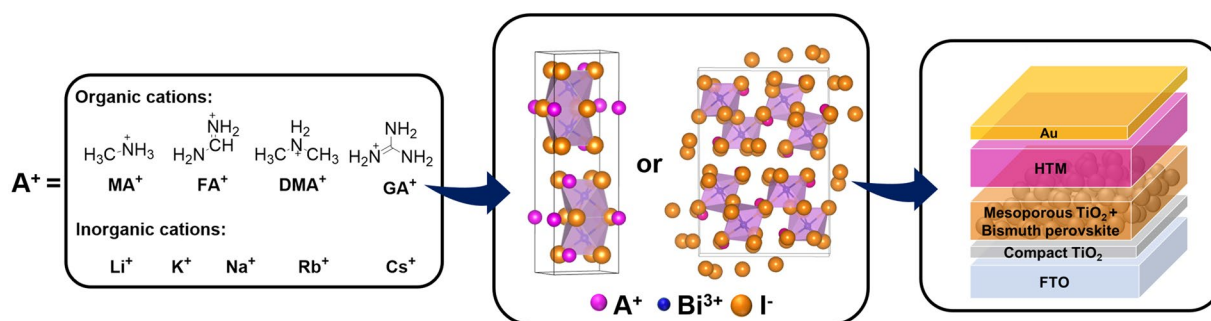

Figure 1: Employed organic and inorganic monovalent cations for the A-site in bismuth iodide perovskite-inspired materials with $A_3Bi_2I_9$ structure for solar cell application.
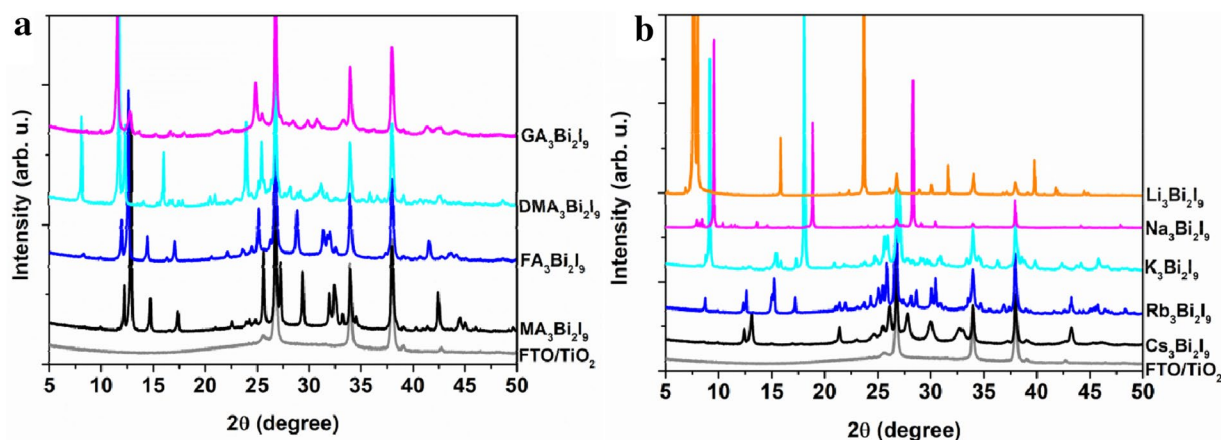
Figure 2: XRD patterns of (a) organic–inorganic and (b) all-inorganic bismuth iodide thin films on mesoporous TiO_2 coated on FTO substrate.

To study the effect of A-site cation engineering on the morphology, all perovskite and non-perovskite ($Li_3Bi_2I_9$) thin films on mesoporous TiO_2 layer (Figs. 4 and 5) were investigated via scanning electron microscopy (SEM). Furthermore, a focused ion beam (FIB-SEM) was used to investigate the cross-sectional profile of the thin films on mesoporous TiO_2 layers (Inset images in Figs. 4 and 5). The top surface morphology of $MA_3Bi_2I_9$, $FA_3Bi_2I_9$, and $DMA_3Bi_2I_9$ showed non-homogeneous dendrite-like morphology, as seen in Fig. 4a, c, e respectively. This can be due to the rapid crystallization of the perovskite material [27]. In the $MA_3Bi_2I_9$ (Fig. 4a) and $FA_3Bi_2I_9$ (Fig. 4c) thin films, the number of grain boundaries is higher due to the preferred orientation along the (101) plane (Fig. 2a) leading to a growth of the plate-like grains perpendicular to the substrate axis. In the case of $DMA_3Bi_2I_9$, the plate-like grains are more parallel to the substrate, which can be a hint for a different crystal structure due to the high ionic radius, leading to the parallel grain growth.

For $GA_3Bi_2I_9$, island growth can be observed (Fig. 4d) on top of the mesoporous layer.

In $Cs_3Bi_2I_9$, the thin dendrite-like grains are perpendicular to the substrate with loose packing leading to a non-uniform thin film on top of the mesoporous TiO_2 (Fig. 5a). The $K_3Bi_2I_9$, $Na_3Bi_2I_9$, and $Rb_3Bi_2I_9$ show grain growth parallel to the substrate, due to the 2D layered crystal structure with a preferential orientation of (00-6) [39]. However, due to the lack of a closed capping layer, which can be observed in the FIB-SEM images (Fig. 5b–d), the top-view SEM images reveal an island-like morphology without any interconnection. This can be similarly observed in the $Li_3Bi_2I_9$ thin film case as shown in Fig. 5e. The obtained organic–inorganic and all-inorganic bismuth iodide thin films show an inhomogeneous morphology. The influence of this crystal growth on the device performance will be discussed below.
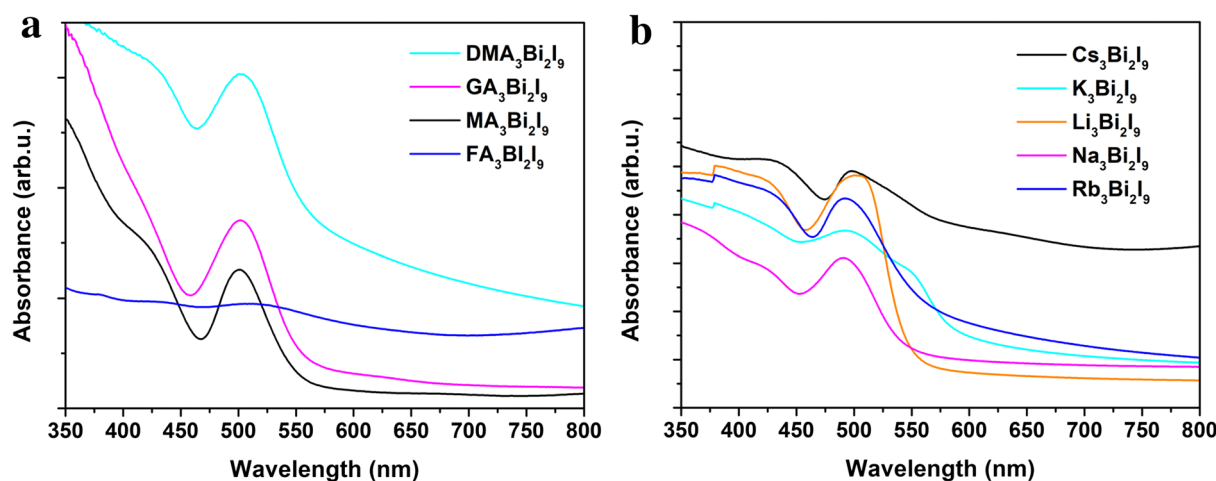

Figure 3: UV–Vis absorption spectra of $A_3Bi_2I_9$ thin films with (a) organic A-site cations and (b) inorganic A-site cations.

To investigate the photovoltaic performance, the perovskite compositions were incorporated in a regular n-i-p perovskite solar cell configuration (Fig. 1) with FTO anode, compact and mesoporous TiO_2 layer as electron transport material (ETM), Li-TFSI and *tert*-butylpyridine-doped spiro-OMETAD as hole transport material (HTM) and gold as a cathode. For $Na_3Bi_2I_9$ and $Li_3Bi_2I_9$ based solar cells, a dopant-free poly(triarylamine) (PTAA) was used as HTM, because the dopants corroded these absorber layers while spin-coating. Figure 6a displays the current density–voltage (*J–V*) curves of the champion organic–inorganic bismuth iodide solar cells measured under simulated one sun conditions (100 mW/cm²). Here, $MA_3Bi_2I_9$ shows the best power conversion efficiency of 0.22% compared to other organic A-site cation bismuth perovskite-inspired material-based devices. The solar cell parameters from champion devices with organic–inorganic bismuth iodides are listed in Table S3 and the box plot of device parameters is shown in

Figure S9. $FA_3Bi_2I_9$ solar cells achieved 0.02% PCE and an open-circuit voltage (V_{OC}) of 0.51 V, which is higher than the previous report for $FA_3Bi_2I_9$ processed from DMF solution [29]. $DMA_3Bi_2I_9$ and $GA_3Bi_2I_9$ show photovoltaic activity, however, the efficiency was low due to the comparatively low short circuit current ($J_{SC} < 0.1$ mA/cm²) and lower $V_{OC} < 0.55$ V. Figure 6b presents the champion *J–V* curves of all-inorganic bismuth halides, where $Cs_3Bi_2I_9$ based solar cells show the best performance (PCE of reverse scan 0.24%, Table S4) compared to rubidium-, potassium- and sodium-based bismuth iodide absorber based solar cells, which showed PCE up to 0.15% (Table S4). In addition to this, a large hysteresis in the *J–V* curve of $K_3Bi_2I_9$ was observed compared to the others as shown in Figure S8b. It can be noted that the hysteresis is higher in inorganic A-site cation based materials compared to the organic-cation ones (Figure S8). Here, $MA_3Bi_2I_9$, $DMA_3Bi_2I_9$, and $FA_3Bi_2I_9$ solar cells showed the minimal hysteresis. Various factors have been reported to
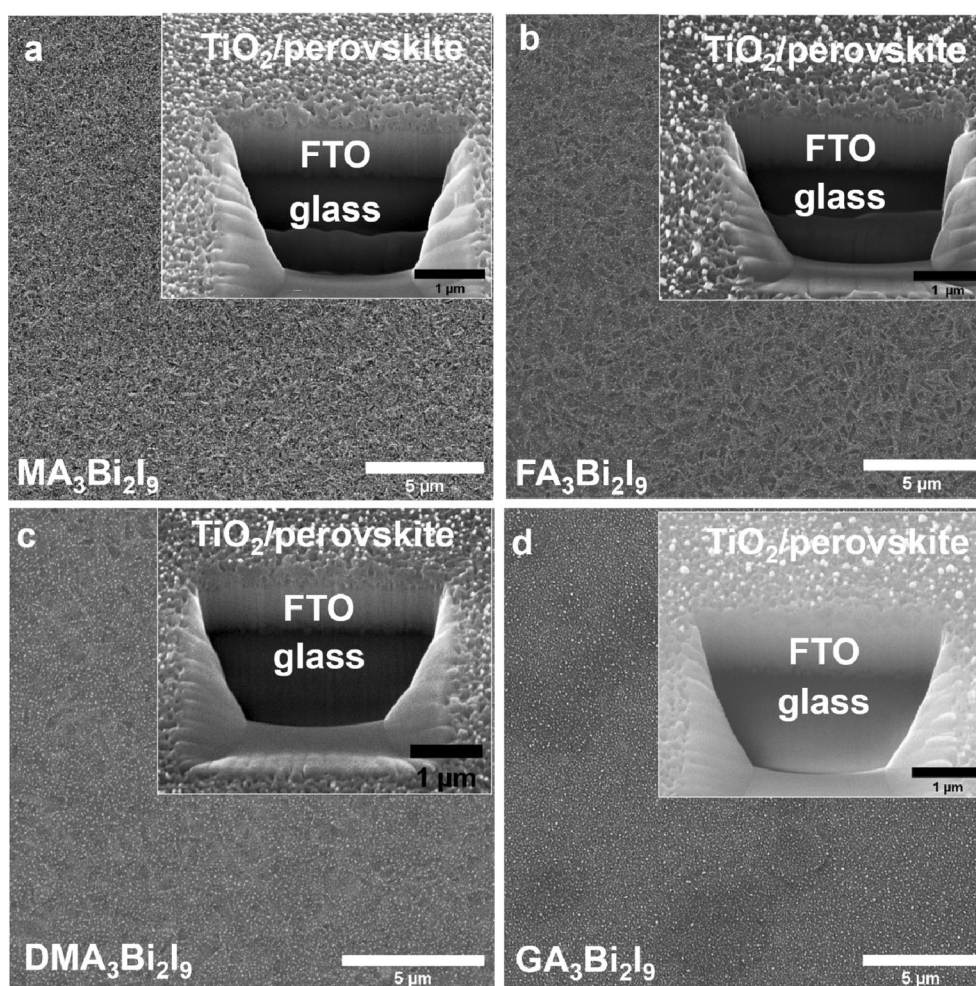

Figure 4: Scanning electron microscopy images of organic–inorganic bismuth iodide thin films on FTO/c-TiO₂/m-TiO₂ substrates. The scale bars on the images are 5 μm. Insets show the related focused ion beam-SEM cross section images, showing the perovskite on the mesoporous TiO₂ on FTO. The scale bars on the inset images are 1 μm.

Figure 5: The scanning electron microscopy images of all-inorganic bismuth iodide thin films on FTO/c-TiO$_2$/m-TiO$_2$ substrates. The scale bars on the images are 5 μm. Insets show the related focused ion beam-SEM cross-section images showing the perovskite on the mesoporous TiO$_2$ on FTO. The scale bars on the inset images are 1 μm.
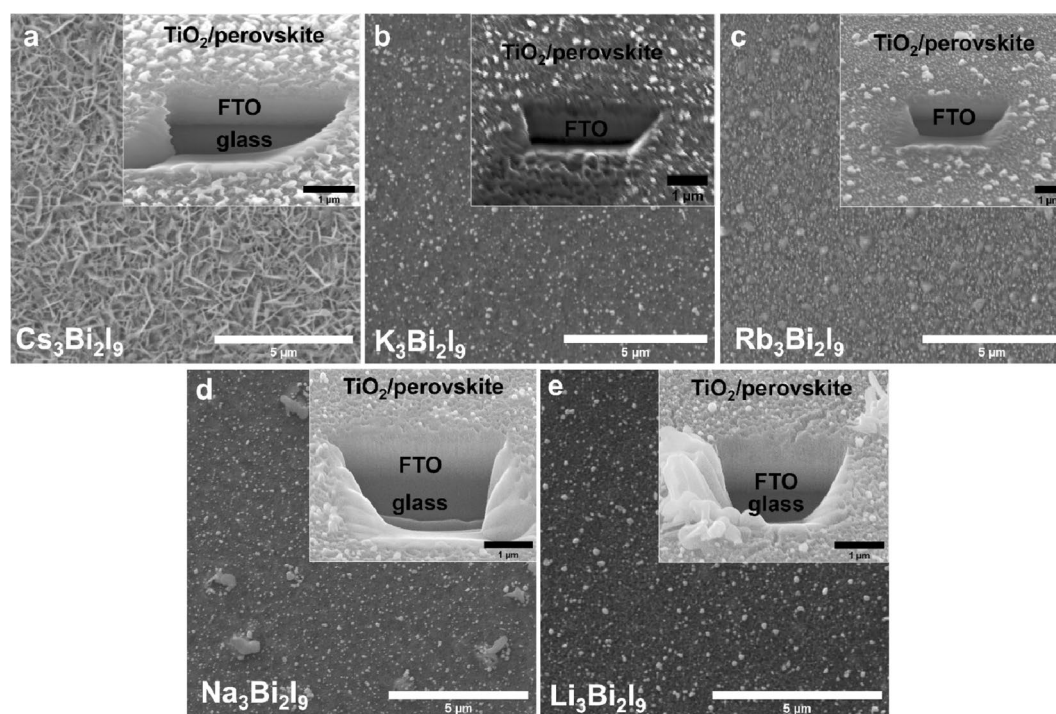
be the reason for hysteresis including ion-migration, ferroelectric effect, etc. [40, 41] We suspect that ion migration arising from bulk and surface defects owing to the rapid crystallization and poor morphology might affect charge transport properties within the bulk and at the interfaces leading to hysteresis. Li$_3$Bi$_2$I$_9$ based devices did not work probably due to the structural mismatch on the A-site because of the smaller size of Li$^+$. Apart from employing Li$^+$ as an A-site cation, the results indicate that the A-site cation substitution with suitable monovalent cations can provide new photo-active compositions and work in the proof of concept solar cell devices. However, the lack of a homogenous capping layer (Figs. 4 and 5) causes an increase of recombination centers at the interfaces between the ETM/perovskite/HTM leading to performance losses. Furthermore, the relatively wide band gaps (> 2 eV, Table S1 and S2) along with the reported high exciton binding energies (up to 300 meV) [24] lead to inefficient charge carrier generation and extraction resulting in lower photovoltaic performances in bismuth based perovskite-inspired materials.

Double-cation based bismuth iodide perovskite

Mixed A-site cation based lead perovskites have shown outstanding properties such as better crystallization and grain morphologies, improved long-term stability, and overall enhancement of optical and photovoltaic properties [9]. Since Cs$_3$Bi$_2$I$_9$

and MA$_3$Bi$_2$I$_9$ led to the best results in our work, we mixed both perovskites to obtain a double-cation bismuth perovskite-inspired materials and investigate their optical, structural, morphological properties and the resultant device performance. According to the previous report, incorporation of cesium (Cs$^+$) in lead iodide perovskites was shown to support the crystallization leading to increased grain sizes along with stabilizing the overall perovskite structure against the thermal influence and gaining reproducibility [42]. Therefore, solutions of Cs$_3$Bi$_2$I$_9$, MA$_3$Bi$_2$I$_9$ and volume mixtures of 2% Cs$_3$Bi$_2$I$_9$ + 98% MA$_3$Bi$_2$I$_9$ (2 mol% Cs), 5% Cs$_3$Bi$_2$I$_9$ + 95% MA$_3$Bi$_2$I$_9$ (5 mol% Cs), 10% Cs$_3$Bi$_2$I$_9$ + 90% MA$_3$Bi$_2$I$_9$ (10 mol% Cs) and 15% Cs$_3$Bi$_2$I$_9$ + 85% MA$_3$Bi$_2$I$_9$ (15 mol% Cs) were prepared and spin-coated using the anti-solvent method for structural and morphological analysis.

The XRD patterns of the cesium alloyed bismuth iodides (labeled as mol.% Cs) and the pristine perovskites (MA$_3$Bi$_2$I$_9$ and Cs$_3$Bi$_2$I$_9$) on mesoporous TiO$_2$ are shown in Fig. 7a. The higher the content of cesium in the perovskite composition the lower are the intensities of the peaks at 2θ = ~ 15°, 17.4° and the doublet at 45° which are assigned to (012), (013), (036), and (029) respectively. An additional small peak appears at 17° belonging to (00-4) orientation, the peak at 21.3° (-120) increases, the peak at ~ 30° is broader and the doublet at ~ 32° coalesce to fit into the pristine crystal structure of Cs$_3$Bi$_2$I$_9$. Additionally, a slight shift towards higher 2θ angles can be seen in the Cs containing compositions due to the smaller ionic radius of Cs$^+$
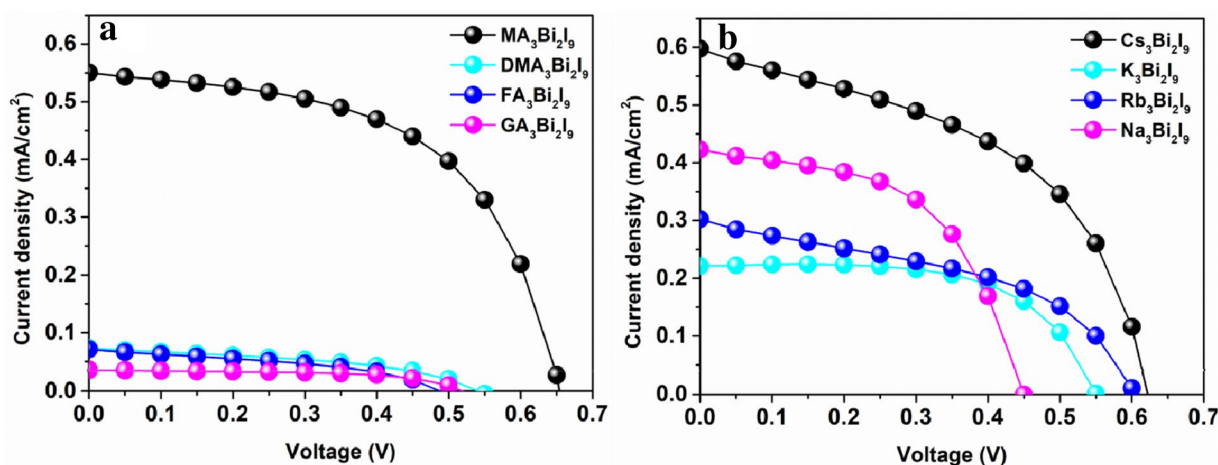
Figure 6: J–V curves of organic–inorganic (a) and all-inorganic (b) bismuth iodide thin films in FTO/c-TiO$_2$/m-TiO$_2$/perovskite/HTM/Au stacked champion solar cells.

(r_{Cs+} = 170 pm vs. r_{MA+} = 217 pm) leading to a decrease of the crystal lattice. We do not observe phase segregation in the Cs$^+$/MA$^+$ based materials since all shown compositions fit the P63/mmc space group with a hexagonal crystal system.

All compounds show an exciton absorption peak at 500 nm, whereby pristine Cs$_3$Bi$_2$I$_9$ had the highest absorption (Fig. 7b). However, we can see a difference in the slope of the absorption maxima. Since the grain morphology was better for 10 mol.% Cs$^+$ (Fig. 7c), we took this composition for further investigation. From Tauc plots, we extracted an indirect optical band gap of 2.1 eV and a direct bandgap of 2.6 eV, which is lower than for the pristine MA$_3$Bi$_2$I$_9$ (Figure S11). The bandgap narrowing is widely known for Pb–Sn compositions [43] and has been recently observed in low-dimensional perovskites with dual metals (Bi and Sb) [44]. However, it is very interesting to observe the bandgap reduction, as observed in the present study, with the mixture of A-site cations in the bismuth-based low-dimensional perovskite. This manifests that the A-site cation mixing in MA$_3$Bi$_2$I$_9$ with Cs influences the bandgap of bismuth perovskite-inspired materials. This observation is in contrast to the previously reported A$_x$Rb$_{3-x}$Bi$_2$I$_9$ perovskite-inspired materials in which the bandgap was insensitive to A-site cation engineering [45].

The impact of the A-site cation mixing on the thin film morphology was investigated by SEM. The SEM images of the pristine and mixed perovskites are depicted in Fig. 7c indicating a change of the initial morphology of MA$_3$Bi$_2$I$_9$. We observe that the biggest grains were obtained for 10 mol% Cs having a hexagonal shape (Figure S11a). The grain size decreases for higher Cs amount and pristine Cs$_3$Bi$_2$I$_9$ leading to the above-mentioned thin plate-like grains. An improved grain morphology and grain size can help to obtain a uniform interface with adjacent transport layers and enhance the solar cell performance.

(Cs$_{10}$MA$_{90}$)$_3$Bi$_2$I$_9$ was incorporated into the FTO/c-TiO$_2$/m-TiO$_2$/perovskite/spiro-OMETAD/Au solar cell configuration. The top-view SEM of the thin film on mesoporous TiO$_2$ and cross-section SEM are presented in Fig. 8a showing that the material is infiltrated in the mesoporous scaffold of TiO$_2$ and there is no thick capping layer. Despite the lack of a uniform absorber capping layer, an efficiency of up to 1.5% was obtained (Fig. 8b) with J_{SC} = 4.0 mA/cm^2. Expecting that a capping layer can increase this performance, we fabricated thin films from a 45 wt% precursor solution. Cross-sectional SEM images, as shown in Figure S12, showed a thick perovskite capping layer, however, the device efficiency was significantly reduced. Recently, Momblona et al. reported on similar observations in co-evaporated highly uniform MA$_3$Bi$_2$I$_9$ thin films, in which a very low PCE of 0.01% was achieved with a thick capping layer [26]. A thick layer of perovskite regardless of uniformity is probably detrimental for efficient charge transport, because of the high exciton binding energies (up to 300 meV [24]) and exciton gap states (see excitonic absorption peaks in Fig. 3) leading to inefficient charge separation [33]. The perovskite infiltrated in a thick mesoporous ETM layer could be beneficially related to a faster transport of photogenerated charge carriers between the ETM and absorber similar to dye-sensitized solar cells [46]. In addition to this, the top view SEM image (inset of Fig. 8a) indicates a more interconnected film growth unlike the previously shown plate-like structures, which probably improves the homogeneity in the interface between perovskite and ETM facilitating better charge transport, thus leading to better J_{SC} and reproducibility. In a different batch, the mixed A-site cation bismuth iodide could achieve an enhancement of solar cell performance compared to MA$_3$Bi$_2$I$_9$ (Figure S13), and the reproducibility of the double-cation bismuth perovskite-inspired material is improved (Figure S14).
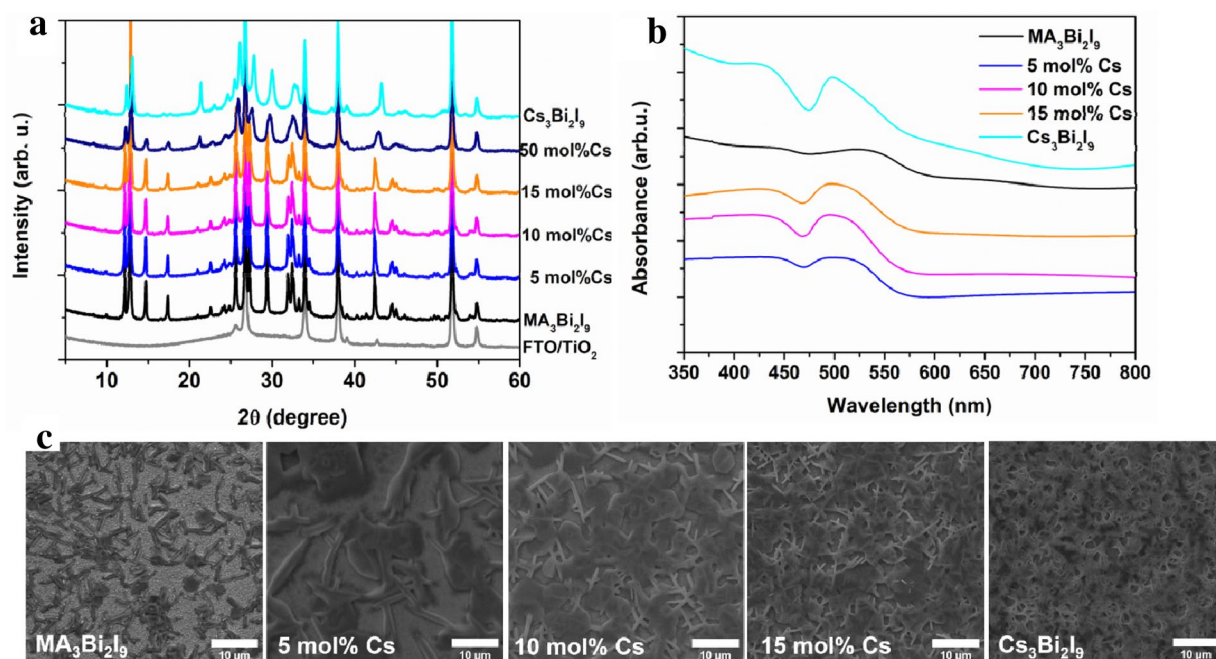
Figure 7: Double-cation bismuth iodide thin films. (a) XRD patterns of $MA_3Bi_2I_9$, mixed compositions with Cs (given in mol%) and $Cs_3Bi_2I_9$. (b) UV–vis absorption spectra of dual-cation perovskites and (c) their morphologies. The scale bar on each SEM image is 10 μm.

Based on our results, we envision that A-site cation engineering in bismuth-based perovskites not only influences the crystal structure and dimensionality of the inorganic framework but can also tune the bandgap. Screening of various cations with compositional engineering can help to reduce the bandgap of low-dimensional bismuth perovskite and perovskite-inspired materials. The A-site cation alloying between Cs and MA shows an improvement in proof of concept solar cell devices and better reproducibility.

Conclusion

In conclusion, our work has highlighted the A-site cation engineering in various perovskite and perovskite-like bismuth iodides for solar cell application. From the X-ray diffractometry analysis, we conclude, that all organic–inorganic bismuth iodides reveal a zero-dimensional dimer structure. All-inorganic bismuth iodides with K^+ and Na^+ are comparable to $Rb_3Bi_2I_9$ having a 2D layered structure, while the Li^+ counterpart could not show any comparable peaks to the other perovskites. The $Cs_3Bi_2I_9$ structure crystallizes in the hexagonal $P6_3/mmc$ space group leading to a 0D dimer structure. The A-site cation variation and mixing between Cs^+ and MA^+ could lead to a reduction in the band gaps, while this was more pronounced for the organic–inorganic and double-cation perovskite. The best single-cation perovskite solar cells were obtained from $MA_3Bi_2I_9$ and $Cs_3Bi_2I_9$, and the mixture thereof leads to improvement in PCE up to 1.5%. The most important limitation lies in the wide

bandgap, the high exciton binding energies and the defective 0D structure of the bismuth halide materials, which must be considered for further research. Furthermore, efforts should be made to develop double A-site cation based perovskites as this might significantly help in tuning the bandgap and transport properties for improved performance.

Materials and methods

Materials

Fluorine doped tin oxide glass substrates (FTO, 8 Ω/sq), titanium dioxide paste (*18NR-T*), methylammonium iodide (MAI), and formamidinium iodide (FAI) were obtained from *Dyesol*. Titanium diisopropoxide bis(acetylacetonate) $(Ti(iOPr)_2(acac)_2)$ 75 wt% in isopropanol, bis (trifluoromethane) sulfonimide lithium salt (Li-TFSI), cesium iodide (CsI), guanidinium iodide (GAI), dimethylammonium iodide (DMAI), lithium iodide (LiI), potassium iodide (KI), sodium iodide (NaI), tert-butylpyridine (TBP), *spiro*-OMETAD and poly(triarylamine) (PTAA) were obtained from *Sigma Aldrich*. Dimethylformamide (DMF), and toluene were purchased from *Acros*. Bismuth iodide (BiI_3) and rubidium iodide (RbI) were purchased from *Alfa Aesar*.

Preparation of thin films

To obtain a 20 wt% perovskite solution, bismuth iodide and the A-site cation iodide were mixed in a ratio of 2:3 in DMF and stirred at room temperature for 1 h. For solution spin-coating,
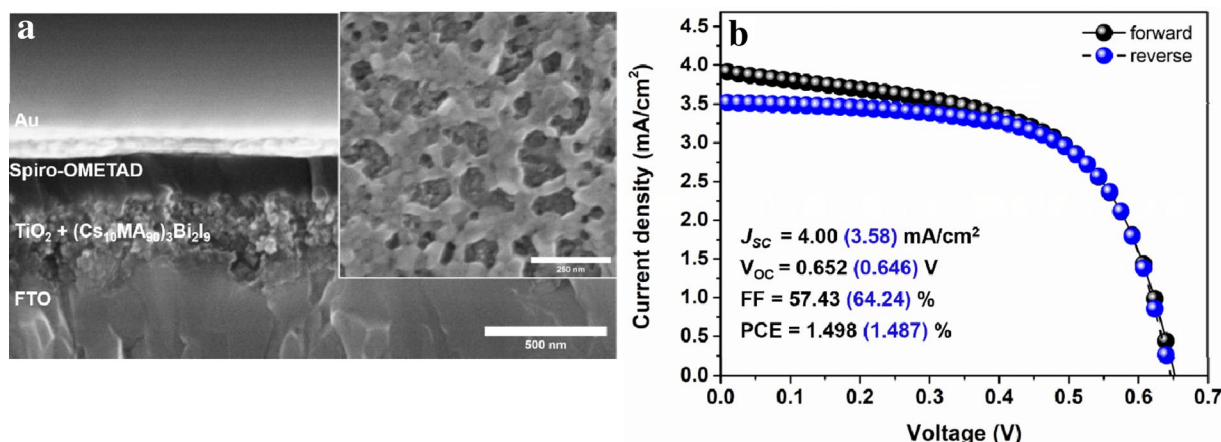
Figure 8: (a) Cross-section and top-view SEM images (inset scale bar 250 nm) of solar cell device with $(Cs_{10}MA_{90})_3Bi_2I_9$ sensitized mesoporous TiO_2. The scale bar is 500 nm. (b) One sun current–voltage curves of the champion device with $(Cs_{10}MA_{90})_3Bi_2I_9$. Forward scan is shown in black and the reverse scan is shown in blue.

a 3-step program was used (1. 2000 rpm, 10 s, 2. 5000 rpm, 25 s, and 3. 6000 rpm, 25 s), in which toluene was used as anti-solvent dripping at the 45th second. The thin films were annealed at 100 °C for 1 h. Thin film and device fabrication was conducted in a nitrogen-filled glovebox.

Device fabrication

FTO substrates (2×2 cm) were cleaned using *Hellmanex III* solution, deionized water, and ethanol in an ultrasonic bath for 15 min each. Before further use, they were kept in a UV-ozone chamber for at least 10 min. For the formation of a compact TiO_2 layer, a spray pyrolysis process was used. A 0.2 M solution of titanium diisopropoxide bis(acetylacetonate) in ethanol was sprayed onto cleaned FTO substrates, preheated up to 480 °C, using a chromatography sprayer (*Aldrich*). After that, the glasses were cooled down slowly to room temperature before putting them into the UV-ozone chamber for 10 min. The FTO/TiO_2 substrates were coated with a solution of TiO_2-nanoparticle dispersion (1:4 wt% in ethanol) to obtain a mesoporous TiO_2 layer. After spin-coating (7000 rpm, 45 s) the glasses were heated at 480 °C for 45 min. 100 μL of perovskite precursor solution was spin-coated using the anti-solvent method and annealed at 100 °C for 1 h. 45 μL of lithium doped *spiro*-OMeTAD (72.3 mg *spiro*-OMeTAD dissolved in 1 mL chlorobenzene, mixed with 28.8 μL TBP and 17.5 μL of a solution of 52 mg LiTFSI in 100 μL acetonitrile) was spin-coated (4000 rpm, 45 s) on the cooled FTO/TiO_2/perovskite layers. For the sodium and lithium bismuth iodide containing devices 35 μL PTAA solution (5 mg/mL in toluene) was used for each substrate and annealed at 60 °C for 10 min. The devices were stored in a desiccator (with 10% humidity and ambient temperature) over night before gold electrode evaporation.

Characterization

The perovskite thin films were measured in a X-ray diffractometer from *Rigaku* with Cu-$K_{\alpha 1}$-radiation ($\lambda = 1.5406$ Å) operated at 40 kV and 20 mA. The surface morphologies of the prepared films were analyzed by scanning electron microscopy (*Nova NanoSEM*, from *FEI* and *SU-8000* from *Hitachi*). FIB-SEM cross section images have been acquired with a *Strata DualBeam 235* from *FEI*, using a 50 pA aperture during milling.

The absorption of the perovskite layers was measured in a *Lambda 950* UV/vis-spectrometer from *PerkinElmer*. The current–voltage (I–V) curves for organic–inorganic and all-inorganic perovskites were measured with *a Keithley 2420 Source Meter* on a calibrated AM1.5 spectrum of a class AAA solar simulator (*WACOM-WXS-140S-Super-L2* with a combined xenon/halogen lamp-based system) providing a power density of 100 mW/cm. The illuminated areas of the cells were 0.15 cm^2 using a mask. The double-cation perovskites were measured with a PEC-L01 solar simulator (Peccell Technologies) with the light intensity of AM 1.5G (100 mW/cm) for current density–voltage measurements of solar cells. The illuminated areas of the cells were 0.032–0.09 cm^2 using a mask for taking the current–voltage curves. All measurements were carried out under ambient atmosphere.

Data availiablity

All data generated or analysed during this study are included in this published article (and its supplementary information files).

Funding

Open Access funding enabled and organized by Projekt DEAL.

Declarations

Conflict of interest The authors declare no conflict of interest.

Supplementary Information

The online version contains supplementary material available at https://doi.org/10.1557/s43578-021-00155-z.

Open Access

References

1. NREL, "Best research-cell efficiencies," can be found under https://www.nrel.gov/pv/cell-efficiency.html, **2020**.

2. A. Kojima, K. Teshima, Y. Shirai, T. Miyasaka, *J. Am. Chem. Soc.* **131**, 6050 (2009)

3. L. Chouhan, S. Ghimire, C. Subrahmanyam, T. Miyasaka, V. Biju, Chem. Soc. Rev. **49**, 2869 (2020)

4. D.W. DeQuilettes, S.M. Vorpahl, S.D. Stranks, H. Nagaoka, G.E. Eperon, M.E. Ziffer, H.J. Snaith, D.S. Ginger, Sci. Rep. **348**, 683 (2015)

5. T. Kirchartz, J.A. Márquez, M. Stolterfoht, T. Unold, Adv. Energy Mater. **10**, 156 (2020)

6. Z. Liu, L. Krückemeier, B. Krogmeier, B. Klingebiel, J.A. Márquez, S. Levcenko, S. Öz, S. Mathur, U. Rau, T. Unold, T. Kirchartz, ACS Energy Lett. **4**, 110 (2019)

7. A. Al-Ashouri, A. Magomedov, M. Roß, M. Jošt, M. Talaikis, G. Chistiakova, T. Bertram, J.A. Márquez, E. Köhnen, E. Kasparavičius, S. Levcenco, L. Gil-Escrig, C.J. Hages, R. Schlatmann, B. Rech, T. Malinauskas, T. Unold, C.A. Kaufmann, L. Korte, G. Niaura, V. Getautis, S. Albrecht, Energy Environ. Sci. **12**, 3356 (2019)

8. R.E. Brandt, V. Stevanović, D.S. Ginley, T. Buonassisi, MRS Commun. **5**, 265 (2015)

9. F. Ünlü, E. Jung, J. Haddad, A. Kulkarni, S. Öz, H. Choi, T. Fischer, S. Chakraborty, T. Kirchartz, S. Mathur, APL Mater. **8**, 070901 (2020)

10. A. Babayigit, A. Ethirajan, M. Muller, B. Conings, Nat. Mater. **15**, 247 (2016)

11. G. Grancini, C. Roldán-Carmona, I. Zimmermann, E. Mosconi, X. Lee, D. Martineau, S. Narbey, F. Oswald, F. De Angelis, M. Graetzel, M.K. Nazeeruddin, Nat. Commun. **8**, 1 (2017)

12. Y. Zhu, S. Poddar, L. Shu, Y. Fu, Z. Fan, Adv. Mater. Interfaces **7**, 2000118 (2020)

13. B. Chaudhary, T.M. Koh, B. Febriansyah, A. Bruno, N. Mathews, S.G. Mhaisalkar, C. Soci, Sci. Rep. **10**, 429 (2020)

14. K. Poorkazem, T.L. Kelly, A.C.S Appl, Energy Mater. Energy Mater. **1**, 181 (2018)

15. N.J. Jeon, J.H. Noh, W.S. Yang, Y.C. Kim, S. Ryu, J. Seo, S.I.I. Seok, Nature **517**, 476 (2015)

16. G.E. Eperon, S.D. Stranks, C. Menelaou, M.B. Johnston, L.M. Herz, H.J. Snaith, Energy Environ. Sci. **7**, 982 (2014)

17. T.M. Koh, K. Fu, Y. Fang, S. Chen, T.C. Sum, N. Mathews, S.G. Mhaisalkar, P.P. Boix, T. Baikie, J. Phys. Chem. C **118**, 16458 (2014)

18. R.E. Beal, D.J. Slotcavage, T. Leijtens, A.R. Bowring, R.A. Belisle, W.H. Nguyen, G.F. Burkhard, E.T. Hoke, M.D. McGehee, J. Phys. Chem. Lett. **7**, 746 (2016)

19. S. Öz, A.K. Jena, A. Kulkarni, K. Mouri, T. Yokoyama, I. Takei, F. Ünlü, S. Mathur, T. Miyasaka, ACS Energy Lett. **5**, 1292 (2020)

20. D. Cortecchia, H.A. Dewi, J. Yin, A. Bruno, S. Chen, T. Baikie, P.P. Boix, M. Grätzel, S. Mhaisalkar, C. Soci, N. Mathews, Inorg. Chem. **10**, 44 (2016)

21. X. Liu, Y. Wang, T. Wu, X. He, X. Meng, J. Barbaud, H. Chen, H. Segawa, X. Yang, L. Han, Nat. Commun. **11**, 1 (2020)

22. G. Nasti, A. Abate, Adv. Energy Mater. **10**, 1902467 (2020)

23. M. Lyu, J.H. Yun, M. Cai, Y. Jiao, P.V. Bernhardt, M. Zhang, Q. Wang, A. Du, H. Wang, G. Liu, L. Wang, Nano Res. **9**, 692 (2016)

24. B.W. Park, B. Philippe, X. Zhang, H. Rensmo, G. Boschloo, E.M.J. Johansson, Adv. Mater. **27**, 6806 (2015)

25. T. Singh, A. Kulkarni, M. Ikegami, T. Miyasaka, A.C.S Appl, Mater. Interfaces **8**, 14542 (2016)

26. C. Momblona, H. Kanda, A.A. Sutanto, M. Mensi, C. Roldán-Carmona, M.K. Nazeeruddin, Sci. Rep. **10**, 1 (2020)

27. A. Kulkarni, T. Singh, M. Ikegami, T. Miyasaka, RSC Adv. **7**, 9456 (2017)

28. S.M. Jain, T. Edvinsson, J.R. Durrant, Commun. Chem. **2**, 1 (2019)

29. C. Lan, G. Liang, S. Zhao, H. Lan, H. Peng, D. Zhang, H. Sun, J. Luo, P. Fan, Sol. Energy **177**, 501 (2019)

30. Z. Zhang, X. Li, X. Xia, Z. Wang, Z. Huang, B. Lei, Y. Gao, J. Phys. Chem. Lett. **8**, 4300 (2017)

31. A.J. Lehner, D.H. Fabini, H.A. Evans, C.A. Hébert, S.R. Smock, J. Hu, H. Wang, J.W. Zwanziger, M.L. Chabinyc, R. Seshadri, Chem. Mater. **27**, 7137 (2015)

32. S. Öz, J.C. Hebig, E. Jung, T. Singh, A. Lepcha, S. Olthof, F. Jan, Y. Gao, R. German, P.H.M. van Loosdrecht, K. Meerholz, T. Kirchartz, S. Mathur, Sol. Energy Mater. Sol. Cells **1**, 20 (2016)

33. B. Ghosh, S. Chakraborty, H. Wei, C. Guet, S. Li, S. Mhaisalkar, N. Mathews, J. Phys. Chem. C **121**, 17062 (2017)

34. T. Li, Y. Hu, C.A. Morrison, W. Wu, H. Han, N. Robertson, Sustain. Energy Fuels **1**, 308 (2017)

35. K. Eckhardt, V. Bon, J. Getzschmann, J. Grothe, F.M. Wisser, S. Kaskel, Chem. Commun. **52**, 3058 (2016)

36. P. Szklarz, A. Pietraszko, R. Jakubas, G. Bator, P. Zieliński, M. Gałazka, J. Phys. Condens. Matter **20**, 45 (2008)

37. T. Kawai, A. Ishii, T. Kitamuha, S. Shimanuki, M. Iwata, Y. Ishibashi, J. Phys. Soc. Japan **65**, 1464 (1996)

38. R.L. Milot, R.J. Sutton, G.E. Eperon, A.A. Haghighirad, J. Martinez-Hardigree, L. Miranda, H.J. Snaith, M.B. Johnston, L.M. Herz, Nano Lett. **16**, 7001 (2016)

39. J.P. Correa-Baena, L. Nienhaus, R.C. Kurchin, S.S. Shin, S. Wieghold, N.T. Putri-Hartono, M. Layurova, N.D. Klein, J.R. Poindexter, A. Polizzotti, S. Sun, M.G. Bawendi, T. Buonassisi, Chem. Mater. **30**, 3734 (2018)

40. Z. Xiao, Y. Yuan, Y. Shao, Q. Wang, Q. Dong, C. Bi, P. Sharma, A. Gruverman, J. Huang, Nat. Mater. **14**, 193 (2015)

41. D. Di Girolamo, N. Phung, F.U. Kosasih, F. Di Giacomo, F. Matteocci, J.A. Smith, M.A. Flatken, H. Köbler, S.H. Turren-Cruz, A. Mattoni, L. Cinà, B. Rech, A. Latini, G. Divitini, C. Ducati, A. Di Carlo, D. Dini, A. Abate, Adv. Energy Mater. **10**, 46 (2020)

42. M. Saliba, T. Matsui, J.Y. Seo, K. Domanski, J.P. Correa-Baena, N. Mohammad, K.S.M. Zakeeruddin, W. Tress, A. Abate, A. Hagfeldt, M. Gratzel, M.K. Nazeeruddin, S.M. Zakeeruddin, W. Tress, A. Abate, A. Hagfeldt, M. Grätzel, Energy Environ. Sci. **2016**, 9 (1989)

43. F. Hao, C.C. Stoumpos, R.P.H. Chang, M.G. Kanatzidis, J. Am. Chem. Soc. **136**, 8094 (2014)

44. S. Chatterjee, J. Payne, J.T.S. Irvine, A.J. Pal, J. Mater. Chem. A **8**, 4416 (2020)

45. U.H. Hamdeh, B.J. Ryan, R.D. Nelson, M. Zembrzuski, J. Slobidsky, K.J. Prince, I. Cleveland, A. Vela-Ramirez, A.C. Hillier, M.G. Panthani, J. Phys. Chem. Lett. **10**, 3134 (2019)

46. P. Pinpithak, A. Kulkarni, H.W. Chen, M. Ikegami, T. Miyasaka, Bull. Chem. Soc. Jpn. **91**, 754 (2018)